Third Semi-Annual Progress Report:

DESIGN AND APPLICATION OF ELECTROMECHANICAL ACTUATORS FOR DEEP SPACE MISSIONS

Submitted to:

NASA
Marshall Space Flight Center EP64
ATTN: Mr. John R. Cowan

Prepared by:

Dr. Tim A. Haskew
Assistant Professor
Department of Electrical Engineering

Dr. John Wander
Assistant Professor
Department of Mechanical Engineering

College of Engineering
The University of Alabama
Box 870286
Tuscaloosa, AL 35487-0286

Reporting Period:
8/16/94 - 2/15/95

BER Report No. 620-163

Tim A. Haskew
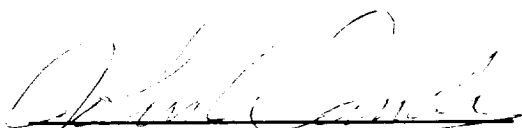Project Director, Co-Principal Investigator

John Wander
Co-Principal Investigator

TABLE OF CONTENTS

I. EXECUTIVE SUMMARY

This third semi-annual progress report covers the reporting period from August 16, 1994 through February 15, 1995 on NASA Grant NAG8-240, "Design and Application of Electromechanical Actuators for Deep Space Missions." Following this summary are two major report sections: Motor Control Status/Electrical Experiment Planning and Experiment Planning and Initial Results. The primary emphasis of our efforts during the reporting period has been final construction and testing of the laboratory facilities. As a result, this report is dedicated to that topic.

I.1. Research Personnel

Over the entire course of this project, three faculty members, eight graduate students, and four undergraduate students have been involved. These individuals, along with their status and funding information, are listed in Table I.1.1.

Table I.1.1. Research Personnel.

Name	Status	Dept.	Funded	Degree Rec.	Comments
T. Haskew	Fac.	EE	Yes	-	
J. Wander	Fac.	ME	Yes	-	
K. Cozart	GS	ME	Yes	-	MS near completion
S. Bhattacharyya	GS	EE	Yes	-	MS near completion
R. Challa	GS	CS	No	MS	
S. Payne	GS	ME	Yes	-	
T. Salem	GS	EE	Yes	MS	PhD in progress
Y.G. Sung	GS	ME	No	-	MS in progress
S. McCarter	UG	EE	No	BS	
S. McGraw	UG	EE	No	BS	
D. Schinstock	Fac.	ME	Yes	-	
F. DeCord	GS	ME	Yes	-	MS in progress
F. Naylor	UG	EE	No	BS	
C. Nielsen	UG	EE	No	BS	
T. Ewing	GS	EE	No	-	MS near completion

In Table I.1.1, the funding column indicates yes if the individual has received any funding from grant funds; this does not imply that funding has been continuous. Please note that Challa and Salem have both completed M.S. degrees through work on this project. Also, Salem is now pursuing the Ph.D. degree, and others are nearing degree completion. The entire EMA research group holds weekly meetings in order to coordinate our efforts and provide students with the opportunity to present their work in a formal setting.

I.2. Technology Transfer

As previously presented, through efforts on this project, two M.S. theses have been written, accepted, and successfully defended:

> Thomas Eric Salem, *Prime Mover Selection for Electromechanical Actuation in Thrust Vector Control Applications*, Master of Science Thesis, The University of Alabama, 1993.

> Ramomohan Challa, *Design of a Computer System to Test Roller Screw Actuators*, Master of Science Thesis, The University of Alabama, 1994.

Additionally, three more M.S. theses are presently in the final stages of preparation:

> Sumit K. Bhattacharyya, *Motor and Control Strategy Selection for Electromechanical Thrust Vector Control Applications*.

> Kris Cozart, *Design and Control of a Roller Screw Test Stand*.

> David Tycyn Ewing, *Brushless DC Machine Controller Design and Testing*.

While theses and dissertations constitute a vital component of technology transfer, publication of research and development findings in technical journals and at technical conferences provides a more effective means for technology transfer to a larger

audience. The following paper was presented at the 27th Southeastern Symposium on System Theory:

> Thomas Salem and Tim A. Haskew, "Simulation of the Brushless DC Machine", *Proceedings of the Twenty-Seventh Southeastern Symposium on System Theory*, March 1995, pp. 18-22.

Additionally, the following paper has been accepted for presentation and publication:

> J. Wander, V. Bird, and J. Parker, "Initial Disturbance Accommodating Control System Analysis for Prototype Electromechanical Space Shuttle Steering Actuator", *1995 American Control Conference*, Seattle, Washington, June 21-23, 1995.

Previously, we have reported three other manuscripts that are in progress. The titles and anticipated journals for submission are provided again below. Completion of these manuscripts will require data from experimentation.

> "Motor Selection for Electromechanical Thrust Vector Control Actuation," *IEEE Transactions on Aerospace and Electronic Systems.*

> "An Adaptive Kalman Filter Approach to Fault Detection in DC Motors," *IEEE Transactions on Energy Conversion.*

> "Numerical Modeling of Disk Springs," *ASME Journal of Dynamic Systems, Measurement, and Control.*

I.3. Final Report Content

With this report being the last that will be submitted prior to the final report on the grant, a tentative summary of the expected final report content is warranted. The final report will be a comprehensive report on all tasks and activities performed or engaged

in during the entire grant period. The following bullet list provides a list of tentative topics to be covered:

- Electric Motor Selection Studies and Guidelines

- Brushless DC Machine Health Monitoring and Fault Diagnosis Prototype Design and Experimental Results

- Detailed Designs of the EMA Test Facility

- Detailed Mechanical Experimental Results

  - Transient Loading

  - Transverse Loading

  - Frictional Modeling

- Detailed Electrical Experimental Results

  - Motor Performance

  - Adaptive Kalman Filter Based Health Monitoring and Fault Diagnosis

  - PWM Strategy Evaluation from an Efficiency Perspective

- Documentation on Simulation Software

II. MOTOR CONTROL STATUS/ELECTRICAL EXPERIMENT PLANNING

The motor drive and speed control loop for the test stand have been previously reported, but are summarized here. Detailed schematics of the motor controller and power electronic drive can be found in the Appendix. The power stage of the drive is IGBT based, and can be seen in Drawing 1. Presently, we have been performing circuit development and prototyping using IGBTs that are underrated to reduce developmental cost. Substitution to appropriately rated devices will be straightforward. The gate drive circuits for one leg of the inverter are shown in Drawing 2. We have chosen to utilize isolation not only on the upper IGBTs, but on the lower ones as well to provide modularity in drive replacement.

Rotor position is sensed by a resolver and resolver-to-digital converter (RDC) system. The output of the RDC is a twelve bit digital word that corresponds to the natural binary angle of the rotor. Comparator logic is used to generate equivalent Hall effect signals as shown by Drawings 3, 4, and 5. The Hall signals are decoded to produce six individual switching signals for the IGBTs. These signals are produced for forward or reverse operation based on a direction bit. This is indicated on Drawing 6. Also on Drawing 6, it can be seen that the lower IGBT switching commands are anded with a PWM signal. Thus, PWM is accomplished using the same six IGBTs as utilized for commutation. The primed switching signals are active high, and they are inverted with open-collector inverters to provide and active low switching signal to the gate drive circuits.

In order to prevent against any logic error or noise problems that may try to turn on both IGBTs in a single leg of the inverter, short-circuit protection has been built in. The protection scheme is shown in Drawing 7, for one leg of the device. The output of

the Q flip-flop is anded with an actual PWM signal such that if Q transitions from high to low, the motor is disabled.

Drawings 8 and 9 represent the PI control and PWM signal generation circuits. The desired speed signal is a -10 to +10 V signal, and the actual speed signal is taken from the RDC on a -4 to +4 V signal. The sign on the desired current is stripped to define the forward/reverse bit, and the absolute value is taken for the current regulation loop.

II.1. Present Status

At the present, the motor is operating under control at reduced power levels and speeds. Input power is derived from a three-phase full-wave bridge rectifier under autotransformer control. To step up to full speed and power operation, The IGBTs must be replaced with ones having sufficient current and power dissipation ratings. Additionally, the snubber circuits may require resizing to limit discharge current rise through the IGBTs. We currently see no difficulty with reaching full operation in time to provide all desired and requested experimental data by the end of the contract period.

II.2. Health Monitoring and Fault Diagnosis

Our efforts on motor health monitoring and fault diagnosis are presently in the process of hardware implementation. A detailed dynamic simulation model of the brushless dc machine under typical fault scenarios has been developed and used as input to the adaptive Kalman filter for filter verification and tuning. Our previous reporting on the Kalman filter approach was aimed at the classical dc machine. Thus, we want

to point out that the extension has been made to a filter that is practical for use with three-phase brushless machines.

The code is presently undergoing final adjustment and verification and will be transported to the ADSP-21020 digital signal processing board in the near future. Additionally, design of the analog electronics for interfacing sensor data to the board is underway. Laboratory procedures for operating the motor under simulated fault conditions are presently under development. A smaller brushless motor is available in-house, and will actually be faulted for experimental purposes.

II.2. Electrical Experiment Planning

Several experimental topics are expected to be investigated prior to completion of the grant period. Three of the more significant items are summarized in the following discussion.

II.2.1. PWM Strategy Evaluation

Four PWM strategies will be evaluated to determine there effects on system efficiency, performance, and possibly thermal management. The PWM strategies to be investigated are hysteresis, triangle, clocked turn-on, and clocked turn-off.

II.2.2. PWM Signal Generation from RDC Output

The 12 bit word output of the RDC provides far greater resolution than is necessary. Thus, for any one switching state, the lower bits in the word cycle many times. Furthermore, the frequency of oscillation of the bits is determined by motor speed. This fact can be used as a tool in PWM signal generation. In typical PWM

applications, the PWM frequency is selected to minimize the dynamic effects of switching on motor speed and torque. Thus, a large number of PWM cycles must occur during one commutation switching cycle. In standard designs, the PWM frequency is chosen high enough to meet this condition when the motor is at top speed and fixed. At lower motor speeds, this frequency is much higher than necessary from a performance standpoint.

If the PWM frequency could be a function of speed, then the ratio of motor speed to PWM frequency could be held constant. In a servo application, this would allow a reduced switching frequency a great deal of the operational duty cycle of the machine. Hence, switching losses could be reduced. This could effectively increase system efficiency and reliability as well as reduce system volume and mass in terms of heatsinks and other thermal management apparatus.

We expect to implement some form of this concept utilizing the RDC output. Efficiency results will be presented from the studies and compared to studies with standard PWM strategies.

II.2.3. Health Monitoring and Fault Diagnosis (HMFD)

The prototype HMFD system will be installed on the testbed and run during typical operation. The results will be analyzed to verify that the system is capable of accurately assessing motor health under nominal conditions under a wide range of dynamic performance specifications. Then, fault simulations will be introduced. The effectiveness of the system to reliably detect major and minor disturbances will be quantified, and the system's ability to accurately quantify machine parameters leading to the failed state will be evaluated.

III. EXPERIMENT PLANNING AND INITIAL RESULTS

As indicated in the previous annual report, the tests to be performed on the roller screw require care in the design of the test stand control system. The models presented in the annual report have been extended to model the hydraulic force control system and have been used in developing appropriate gain selections for the different experiments. In addition, the roller screw modeling equations presented in Section III.1 of the previous annual report were implemented in MATLAB™ and used to guide the gain selections for the in-house motor controller. Initial use of the hydraulic system gives some insight into the backdrive loading required to initiate motion of the screw.

III.1. Implementation of the Electro-Mechanical Test Stand Modeling Equations

The general modeling equations presented in the previous annual report were implemented in MATLAB™ so that simulations could be performed. A schematic of the system used to define the model is shown in Figure III.1. In addition, a PI motor speed controller was added to the system to
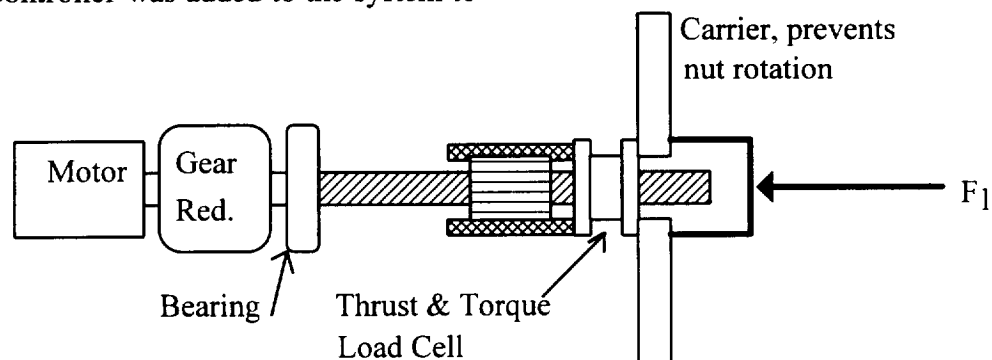
Figure III.1. Test Stand Schematic.

An angular form of the general modeling equation is repeated here with clarification for convenience (refer to Eq. III.3 of 1994 Annual Report):

$$(J_m + g^2 J_s + (gP_h)^2 M_l)\dot{\omega}_m + (B + K_t K_b / R_a)\omega_m = \frac{2\pi g P_h F_l}{\eta_g \eta_r} + \frac{K_t E_{in}}{R_a} \tag{III.1}$$

where:

J_m is the inertia of the motor and the gear reduction referred to the motor shaft,

g is gear reduction between motor and screw,

J_s is screw inertia and the inertia of the nut rollers referred to the screw shaft,

P_h is screw lead (linear/revolution),

M_l is the mass of components that move linearly including the nut and carrier,

B is a viscous loss term associated with the motor angular motion,

ω_m is the angular velocity of the motor,

V_l is the linear velocity of the load-end of the actuator,

K_t is the torque constant of the motor,

K_b is the back EMF constant of the motor,

E_{in} is the effective DC voltage applied by the control system

F_l is the force applied to the end of the actuator, that measured by the load cell.

η_r is the efficiency of the roller screw expressed as a value for 0 to 1.

η_g is the efficiency of the gear reduction expressed as a value for 0 to 1.

These equations are complicated by the essentially nonlinear efficiency model of the energy losses associated with the transmission elements. The efficiency terms η_r and η_g in the equation above represent the efficiencies of the gear and roller screw transmissions assuming that energy flows into the actuator system at the motor and out of the system at the point of linear load application. In these equations, the η terms will move between the numerator and the denominator as the direction of energy flow changes at the motor or the linear load. As shown, the inefficiencies increase the

effective load that the motor is driving against and hence increase the required motor torque.

Though the motor controller is implemented as a current controller at a low level, the gains for the system were originally designed for a voltage controller. Once gains were determined that would work well with the voltage controller structure, it was possible to develop the added circuitry needed to transparently implement the current control underneath the voltage control.

Simulation results demonstrating the ability to generate motion profiles similar to the SSME TVC mission profiles are presented below. These results indicate that the motor acquired for the test stand can operate in the regimes necessary to test roller screws under SSME-like conditions. The mission simulation profile planned is based on the typical mission displacement profiles for the SSME. Figure III.2 demonstrates the ability of the motor/gear reduction system to drive the roller screw provided by NASA against a 25,000 load at 5 inches per second. The figure actually shows only 8 seconds of a longer mission simulation made up of a similar motion repeated several times. The main difference between the motion of Figure III.2 and the intended experiment motion is that the slow-stroke section will be a full extension rather than a short extension. The transitions between forward and backward motion are smoothed by using a smooth input command to prevent discontinuous velocity commands.
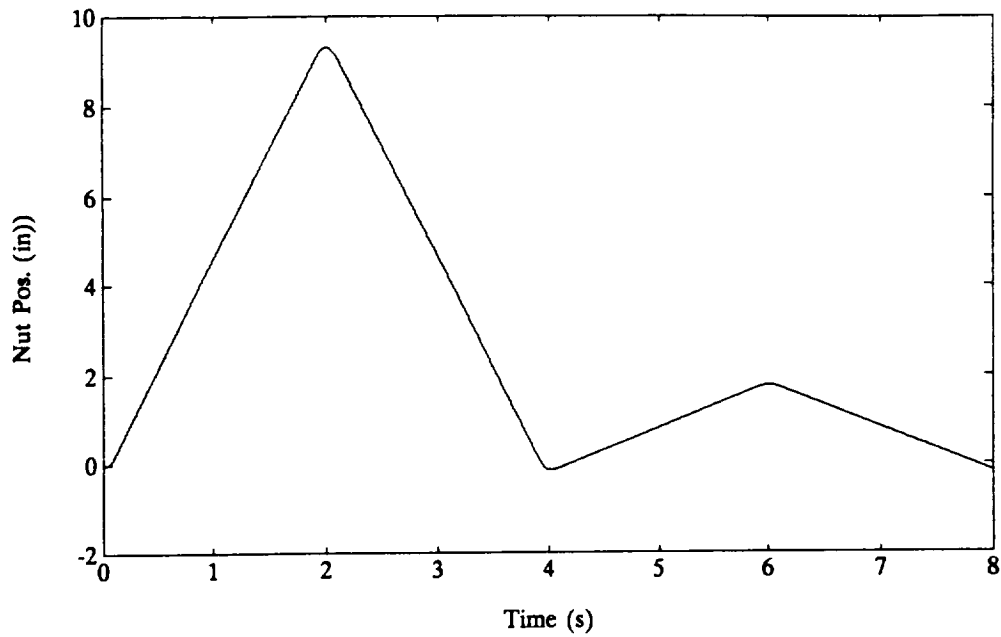
Figure III.2. SSME Mission Simulation Results Based on Test Stand Hardware.

III.2. Hydraulic Actuation Modeling

For both the shock loading and mission simulation experiments, the hydraulic loading system may be force controlled rather than position controlled. Since force control systems often exhibit unstable behavior, a model of the hydraulic system was developed for use in helping to design the control system. A schematic of the physical elements of the system including hydraulics is shown in Figure III.3 below. The model of this system was developed by adding a model of the hydraulic system to the previously developed model of the motor and screw portions of the test bed.

III.4

Motor and Reducer

Load Cell

Nut

Carrier and Cylinder Mass

Cylinder

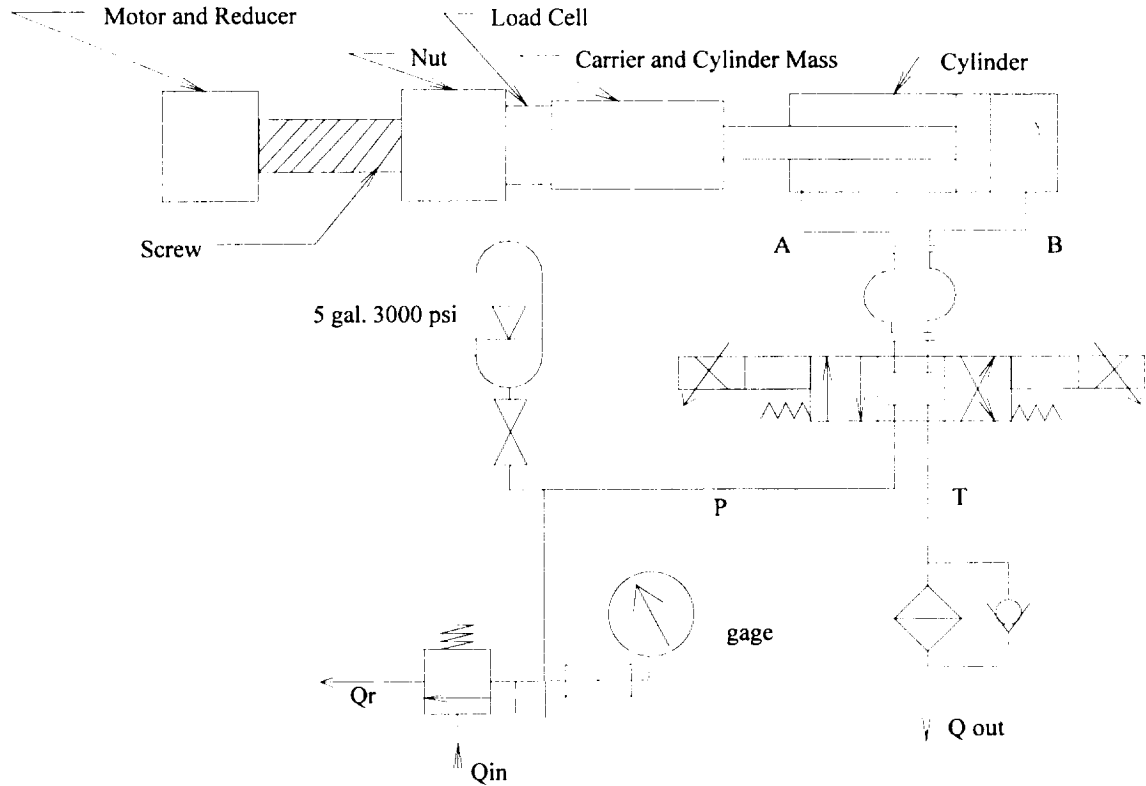Screw

A

B

5 gal. 3000 psi

P

T

gage

Qr

Q out

Qin

Figure III.3. Test Stand Model with Hydraulic Elements.

The pump is modeled as a flow source. The relief valve is modeled as a nonlinear resistance to flow between the accumulator and the reservoir. Performance characteristics provided by the relief valve manufacturer provide a graph of flow vs. pressure for our valve. The relationship between flow and pressure drop across the relief valve can be simply and accurately estimated by a pair of piece wise continuous linear approximations valid above the relief valve setting pressure P_S:

$$Q_r = \begin{cases} 0 & ; \ P_a < P_s - 200 \\ m1(P_a - (P_s - 200)) & ; \ P_s - 200 < P_a < P_s - 100 \\ m2(P_a - (P_s - 100)) & ; \ P_s - 100 < P_a \end{cases}$$

(III.2)

The N_2 charged accumulator was modeled assuming isentropic compression of an ideal gas. By assuming the pressure of the fluid equals the pressure of the gas, the ideal gas law can be written:

$$P_a = \frac{C_g}{(V - V_a)^{1.4}} \tag{III.3}$$

where:

C_g is a constant based on the accumulator initial N_2 charge,

V_a is the volume of oil in the accumulator, and

V is the total volume of the accumulator.

The flow of oil between the accumulator, the cylinder and the reservoir is controlled by the valve, pipe losses and the differential pressures. The actual length of pipe in any flow path is a combination of the appropriate pair of the four separate pipes: P, T, A, and B shown in Figure III.3. For a given volumetric flow through a particular pipe the flow will be either laminar, turbulent, or both. Relations exist to calculate pressure drop for either a purely laminar or turbulent flow. When flow is in the transition region between laminar and turbulent, the pressure loss is bounded on the low side by the laminar loss and on the upper side by the turbulent loss. By determining the pressure drop in each pipe over a range of estimated flow rates, a 2nd order curve fit can estimate the relationship. The pressure losses for a representative section of pipe are indicated in Figure III.3. By fitting a single second-order polynomial both sets of data, equations are derived for each pipe:

$$\Delta P = C_1 Q^2 + C_2 Q \tag{III.4}$$

When the valve is either left or right-of-center, pressure loss coefficients for the appropriate pairs of pipes (P and B for example) can be added to those of the valve to determine flow from the existing pressure differential across the pipes and the valve.
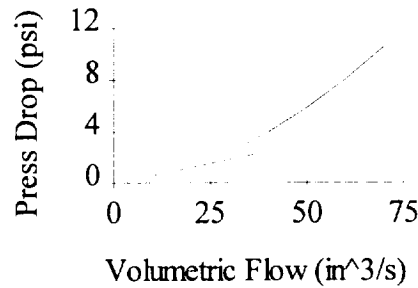
Figure III.3. Laminar and Turbulent Flow Losses for Representative Pipe.

The pressure drop across the servo valve can be estimated from manufactures specifications to be a function of both the servo position, UXa, and the flow rate:

$$\Delta P = C3\left(\frac{1}{UX_a}\right)^2 Q^2 \qquad \text{(III.5)}$$

where:

ΔP is the pressure drop across one of the valve paths,

$C3$ is the coefficient obtained from Bosch literature on the servo valve,

UX_a is the position of the spool valve away from center, and

Q is the volumetric flow rate through the valve.

Holding UXa constant in this equation, one has an additional coefficient in the square of the flow that can be added to coefficients for the pipe loss and used with the differential pressure to solve for the flow rate. Note that the acceleration of the fluid is not being considered in this formulation. The oil is assumed to flow at the equilibrium rate for the differential pressures that exist. An alternative model would include the acceleration required of the oil.

The differential pressures used in the solution for flow rate are those between the accumulator and cylinder and between the cylinder and the reservoir. There is an additional pressure drop across the return filter on the way to the reservoir that

III.7

contributes coefficients to this pressure loss equation just as the pipes do. Pressure in the accumulator has already been discussed. Pressure in the reservoir is atmospheric or gage zero (0). The pressures in the cylinder on both the blind and rod ends are modeled based on bulk modulus compression of the oil. The compression equation is complicated by the fact that the uncompressed volume of oil is changing as is the amount of compression. The uncompressed volume (the volume the oil requires at atmospheric pressure) is used as the reference volume. For instance, in the blind end:

$$P_b = \left(\frac{V_b - A_b x}{V_b}\right)\beta \qquad \text{(III.6)}$$

where:

Pb   is the gage pressure in the blind end,

Vb   is the uncompressed volume of oil in the blind end,

Ab   is the area of the blind end,

x   is the distance between piston and blind end cap, and

β   is the bulk modulus of the oil.

The servo valve dynamics govern the position of the spool, UXa, required in Eq. III.5 above. The dynamics of this portion of the control system are described graphically by the vendor with frequency response plots for the spool position. The input to the servo valve is UXd, the desired servo valve position, as produced by the controller. The frequency response of the servo valve is shown to be a function of the amplitude of the input by the presence of two separate curves, one for 5% input, the other for 100% input. An initial approximation for these dynamics is a second-order model with a damping ratio of 2 and a natural frequency of 50 Hz. Once the actual valve excursions required for a simulation are determined it may be desirable to refine this approximation toward one or the other frequency responses.

A more exact model for the servo valve may be implemented that includes the rate limits associated with the pilot operation of the servo valve. Discussions with Bosch engineers have led to the conclusion that the modulation of response by the magnitude of the input can be modeled in this way.

The control for the servo valve is implemented in analog on a stand-alone controller called a "PQ Card" by the vendor. The "PQ" designation indicates that the card can control either pressure or position. The actual control command that is sent to the valve solenoid always commands spool position. The pressure control portion of the PQ Card is implemented with the circuit shown in Figure III.4 below and is used to form a spool position command. Input signals Eps and Epa are voltages proportional to the desired and actual pressures respectively.
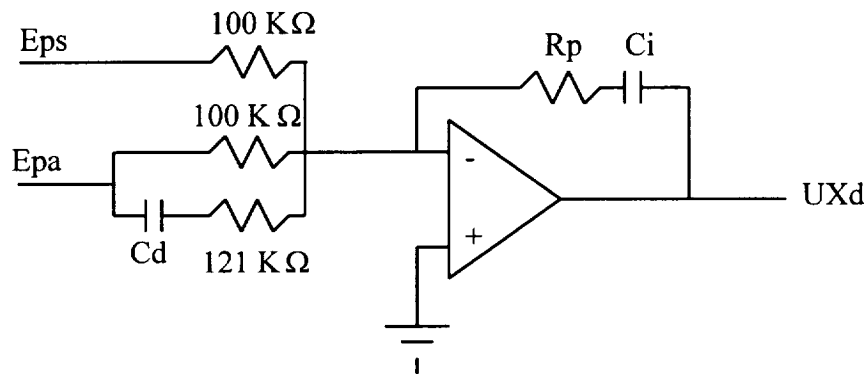
Figure III.4 - Schematic of Force-Control Portion of PQ Card.

The PQ Card is designed to take a pressure error signal minus a high-passed portion of the actual pressure and apply a PI control action to this quantity. The subtraction of the high-passed portion of the actual signal is intended to reduce pressure variations and promote stability. The output of the integrator is limited to prevent integrator windup due to insufficient control authority. In the experiments performed

for force control purposes, the pressure signals will be replaced by force signals. The control action of this controller can be described by the state equations:

$$\dot{E}_d = (K\,P_{act} - E_d)\,/\,(121000*C_d)$$
$$\dot{E}_i = (i\,/\,C_i)$$
$$= \frac{1}{C_i}[\frac{K(P_{act} - P_{set})}{100000} + \frac{(K\,P_{act} - E_d)}{121000}]$$
$$E_o = -(R_p i + E_i) \hspace{4cm} \text{(III.7)}$$

In these equations K is the gain between actual and desired pressures and the input signal voltages. These voltages are constrained to lie between 0 and 10 volts. Note that the saturation of the integral action (E_i) is not reflected in the above linear equations but can be implemented numerically if the state should grow too large by setting the derivative to zero in such cases. Here the output voltage is connected to the input of the position control portion of the PQ Card. If the card is operating as a pressure controller, this signal is passed out directly as the spool position command, UXd, referred to above. The modeling equations developed in this section were used to replace the previously specified hydraulic force in the model of the roller screw and motor discussed in Section III.1. The full set of equations constitutes a model of the entire test stand that can be used for control design.

III.3. Full Simulation and Gain Selection

With the full model equations, the gains for the hydraulic force control system can be designed through simulation. Using conventional PID parameter selection procedures based on step responses, gains for the PQ card were selected as follows:

$$Rp = 300,000 \text{ ohms}$$

$$Cd = 10e\text{-}9 \text{ Farads}$$

$$Ci = 120e\text{-}9 \text{ Farads}$$

One other parameter of interest in these simulations is the time allowed for velocity reversal. As indicated in Section III.1, the input is shaped to prevent a discontinusous change in desired velocity. A sine function is used to smoothly change between any pair of desired speeds with either pi or pi/2 being mapped onto a time increment of ΔT. This is the time it takes to go from a constant velocity in one direction to the same velocity in the opposite direction. With the above gains and a ΔT of 0.8 seconds, the model presented above indicates a maximum force error of +/- 4000 pounds while commanding a constant force of 28,000 and the nut displacement shown in Figure III.2.. The displacement history obtained through simulation is shown in Figure III.6. Both the desired and actual achieved forces are shown in Figure III.7. Lowering ΔT results in a greater acceleration of the nut and a larger force error caused by dynamic effects in the hydraulic system. Simulation indicates that values of ΔT below 0.6 seconds will cause a vacuum to occur in the rod end causing a risk of cavitation that is very undesirable. As per design, the fast stroke causes fluid levels in the accumulator to drop. During the slow stroke fluid is returned to the accumulator so that full working pressure is again obtained at the beginning of the next cycle.

Similar simulation results are being developed for the shock loading experiment. In addition, the force control with the gains chosen above is being implemented on the test stand.
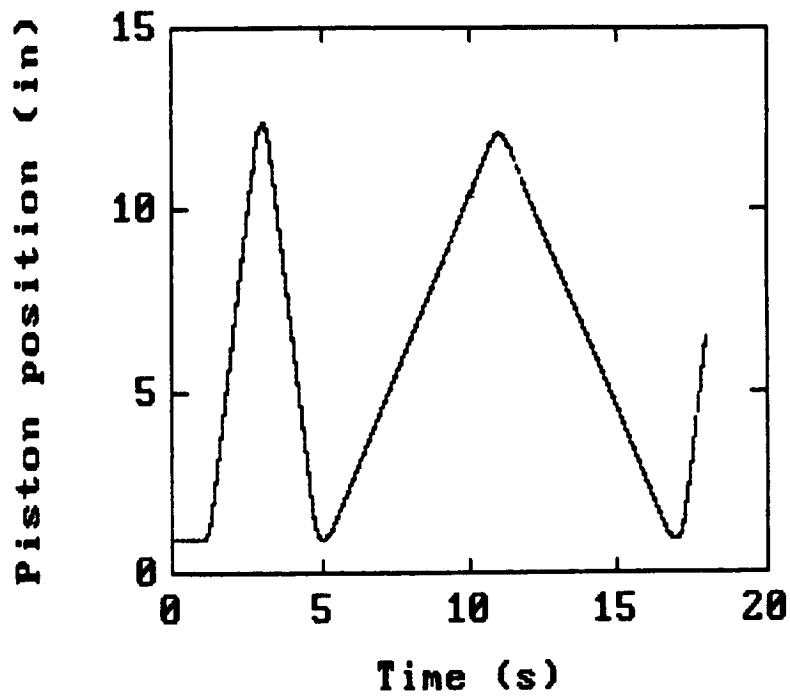
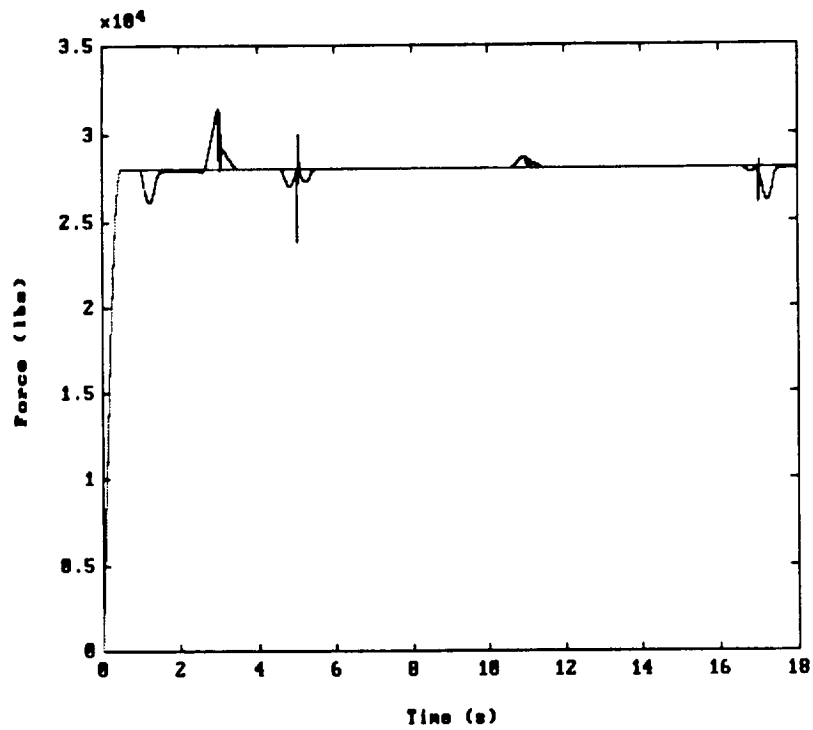Figure III.5 - Simulated Displacement Including Hydraulic Force Control.

Figure III.6 - Actual and Desired Force Predicted by Simulation.

III.4. Initial Results

Initial results for the loads required to backdrive the roller screw have been obtained. In these plots the data is only partially calibrated. The horizontal axis is a time axis but uncalibrated so the unit is sample number. The total period shown in both Figure III. and Figure III.8 is approximately 2 seconds. There is a constant bias error on the load traces (shown with the heavier lines). One can assume that the the mean value of the load is actually close to zero. The position (shown with the lighter lines) is the position of the nut along the screw measured with respect to an arbitrary position along the screw.

The displacements in each case were generated using the hydraulics in a position control mode. The screw was left passive with only the gear reduction inertia to increase acceleration loading. The loads generated by acceleration or friction of the carrier are not measured by the load cell. Observation of these results indicates that there is a Coulombic load of approximately 1000 lbf. This result is consistent with earlier tests done with a hydraulic ram though the resolution of this result is poor. In addition, judging from the relatively small change in the load due to a factor of four increase in the peak speed of the nut indicates a weak friction load dependence on speed. Loads associated with the acceleration itself are not visible in this data. Additional data with more extreme position profiles forced on the nut is being collected.
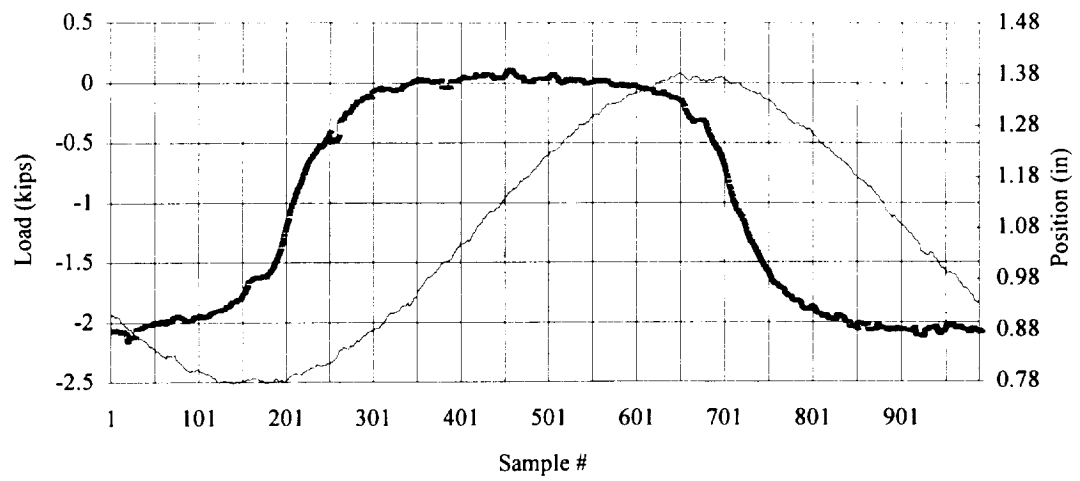
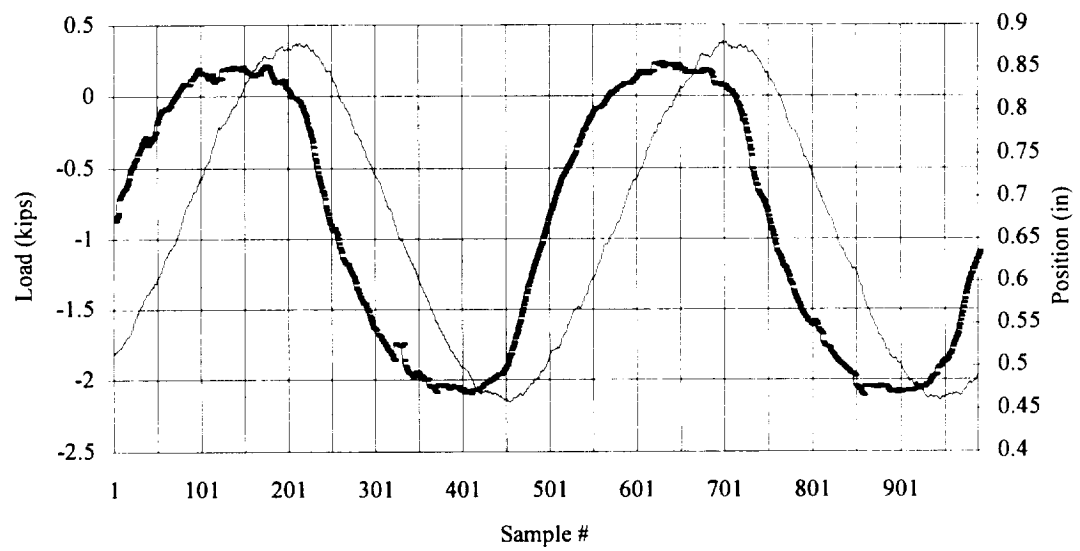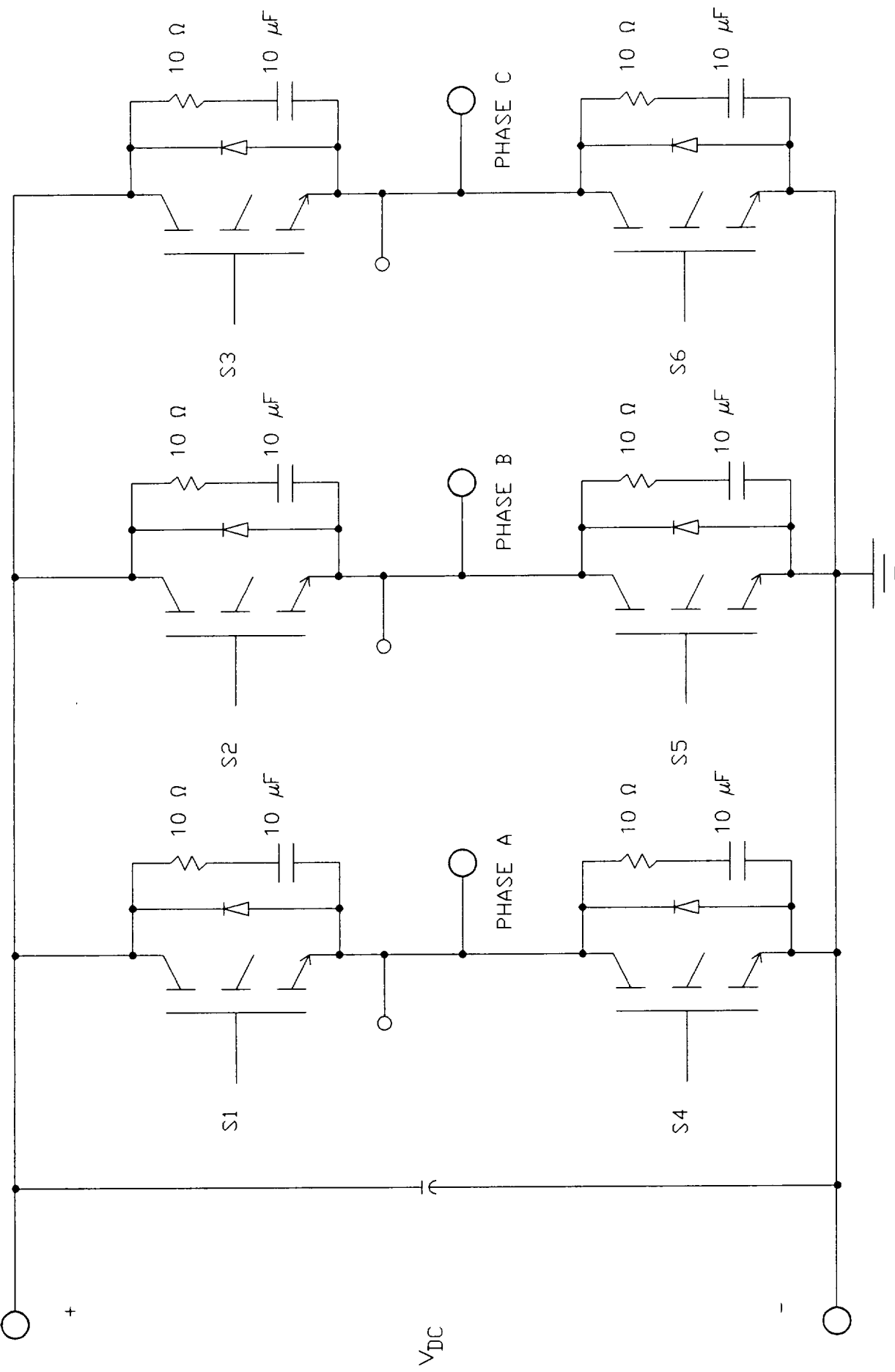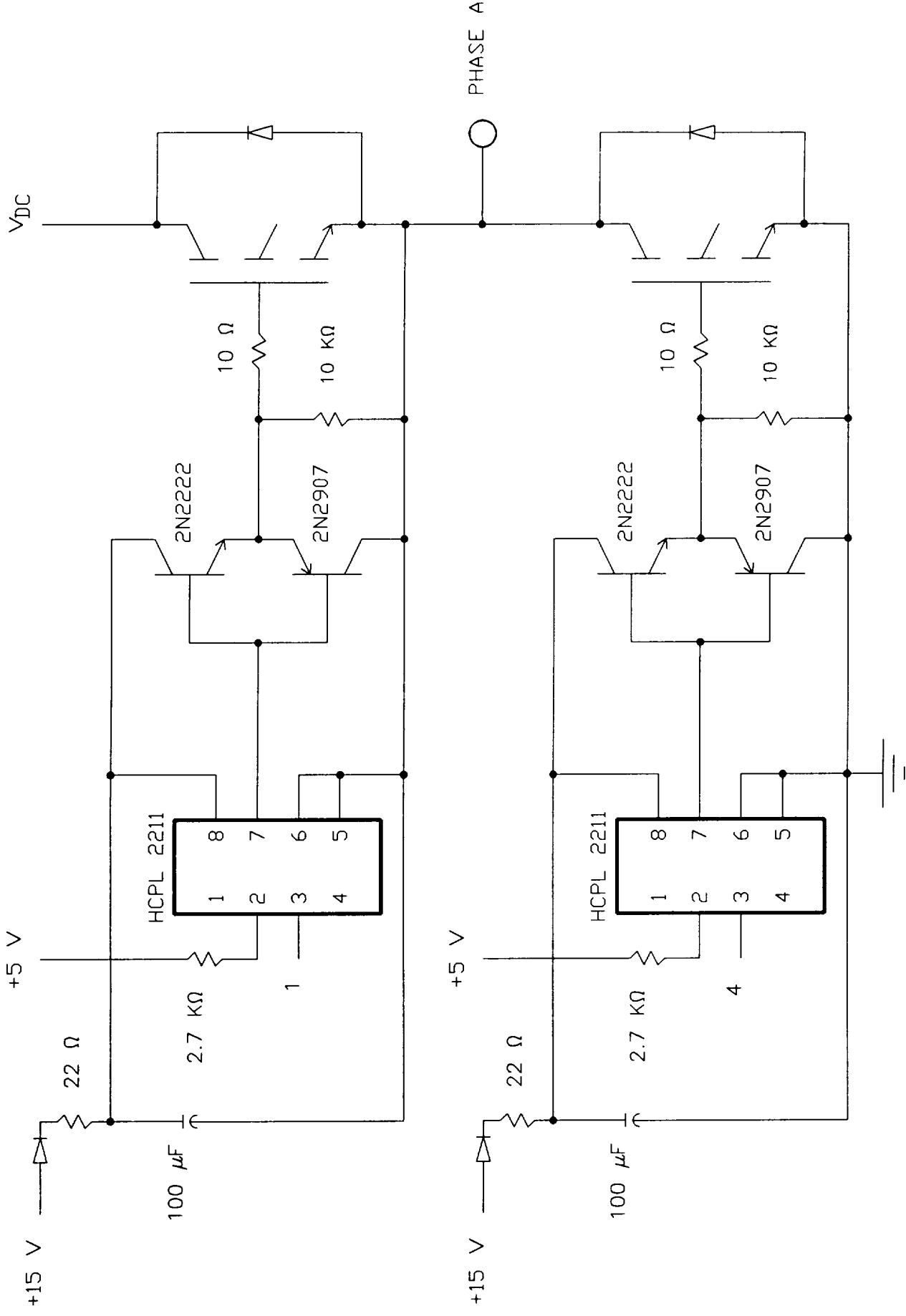Figure III.7 - Loads and Positions During Hydraulic Backdrive of Screw.

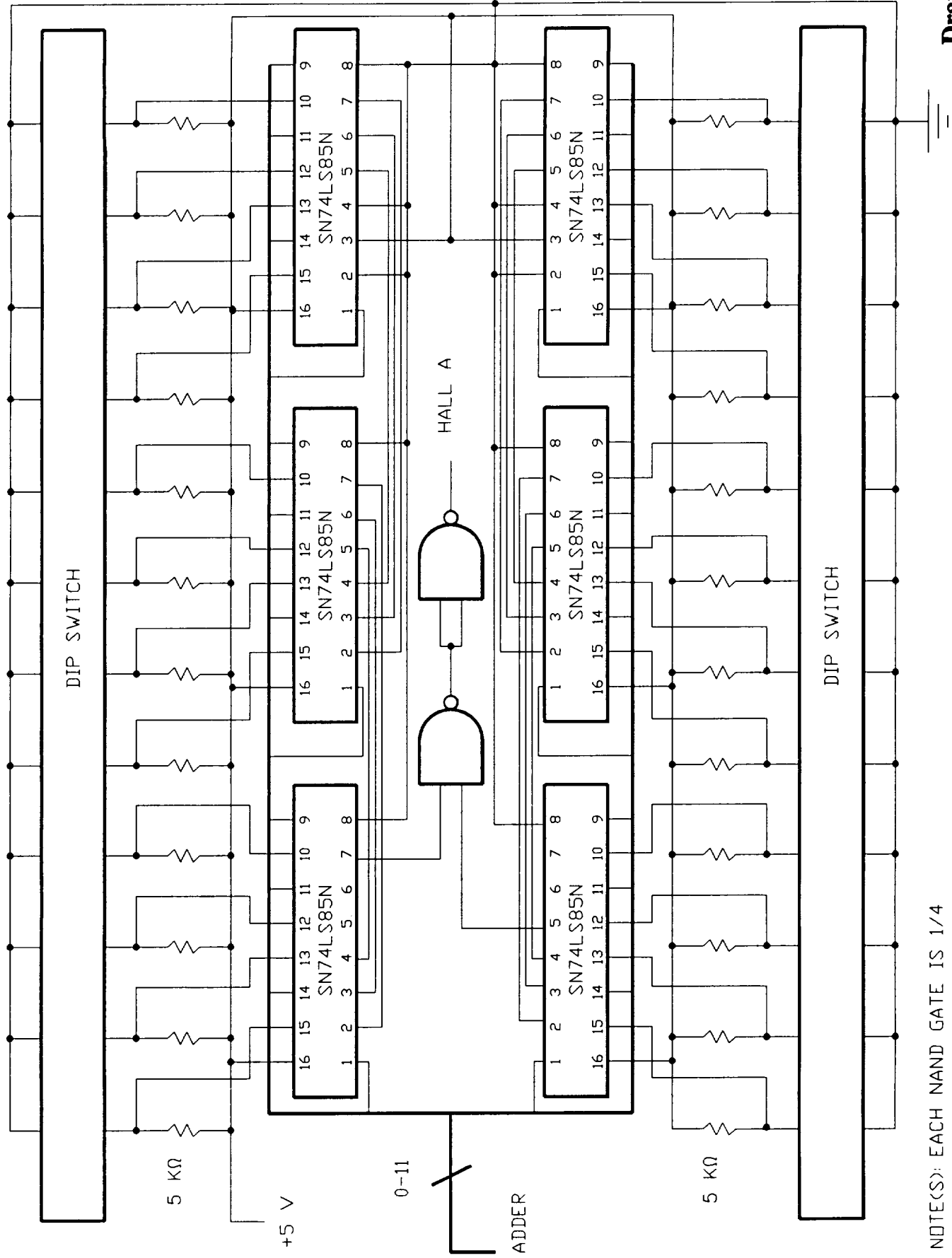Figure III.8- Loads and Positions During Hydraulic Backdrive of Screw.

III.14

APPENDIX

Motor Controller/Drive Schematics

Drawing 1

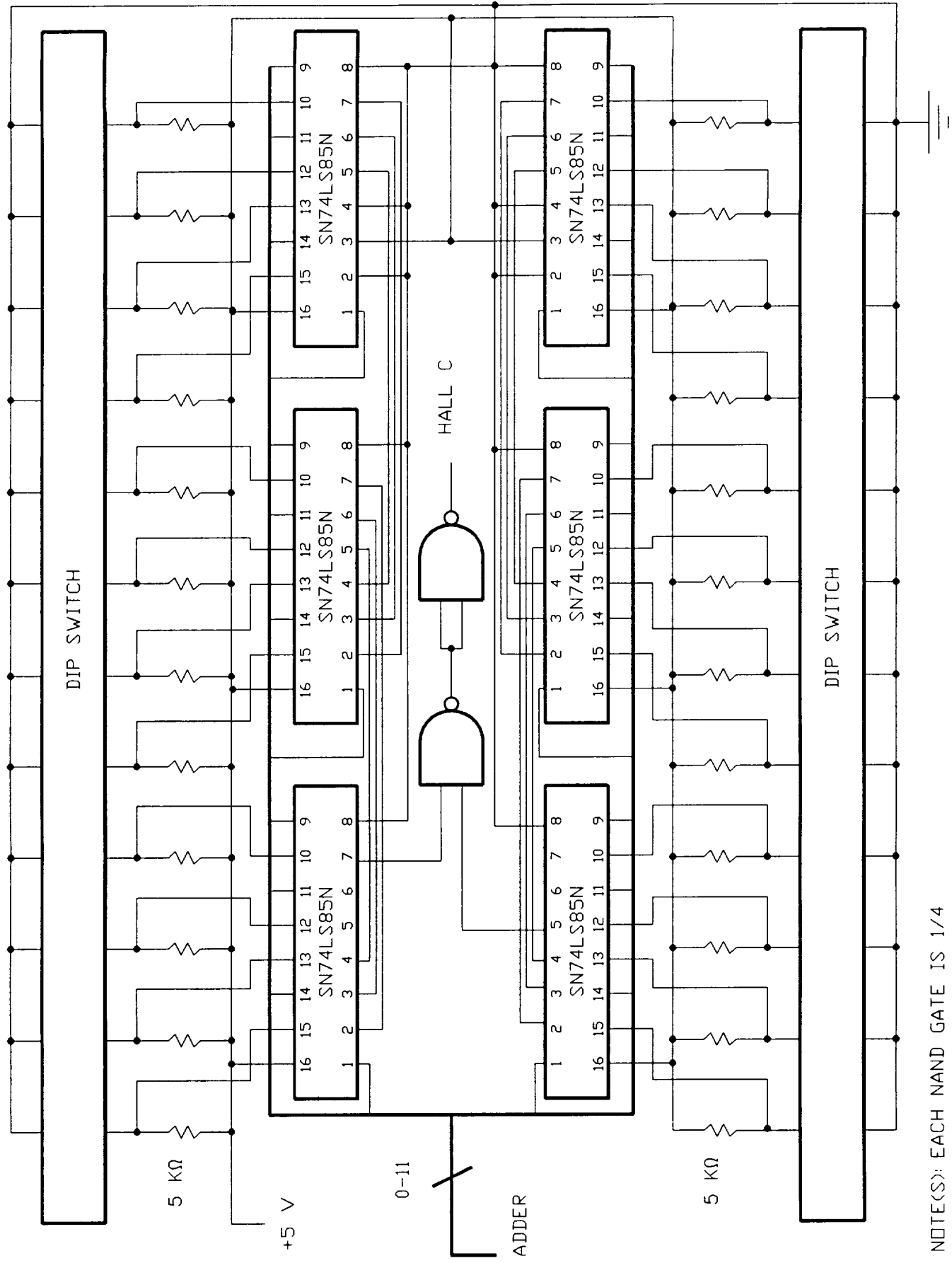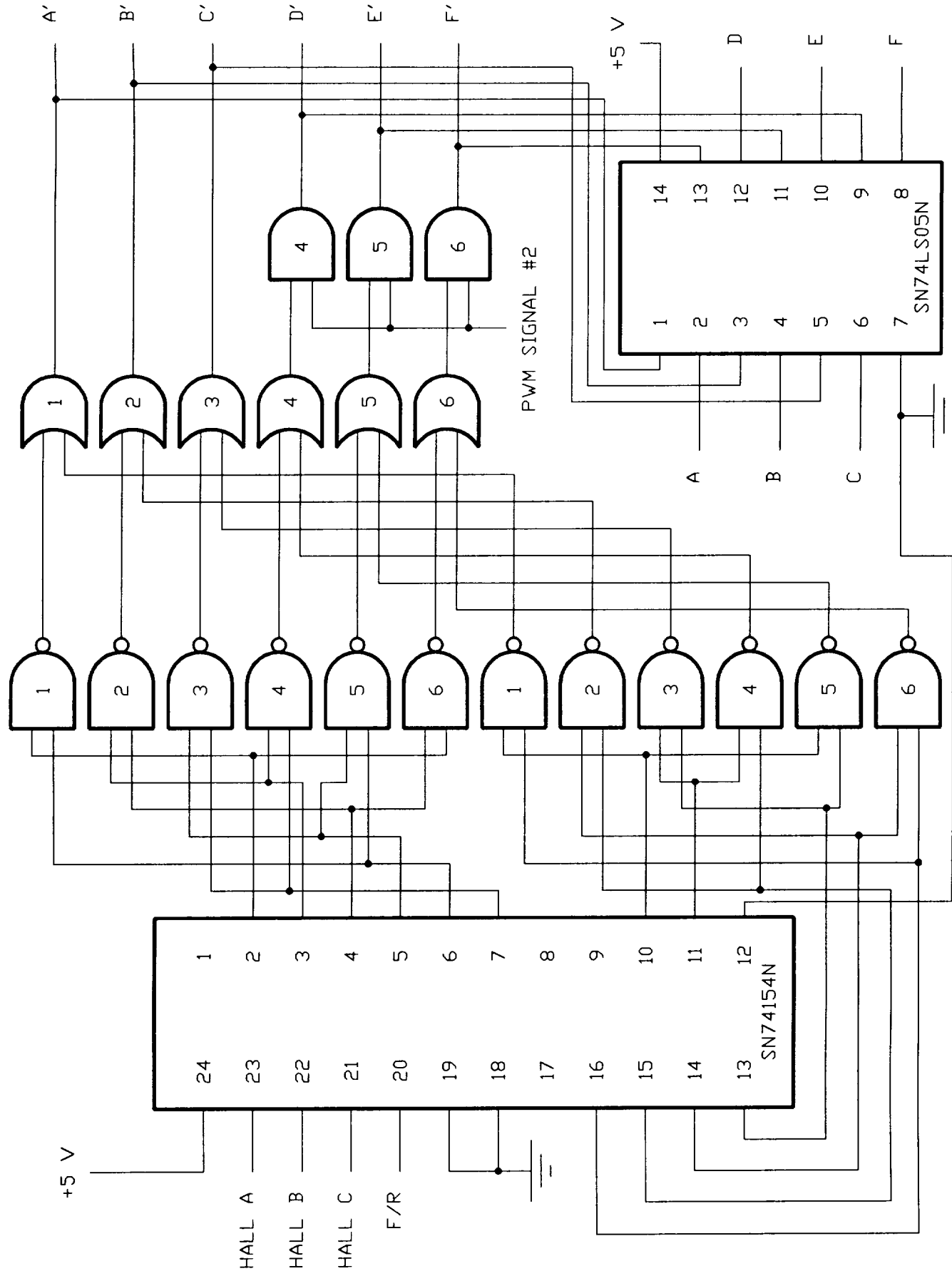**Drawing 2**

Drawing 3

DIP SWITCH

SN74LS85N

SN74LS85N

SN74LS85N

HALL A

DIP SWITCH

SN74LS85N

SN74LS85N

SN74LS85N

5 KΩ

+5 V

0-11

ADDER

5 KΩ

DIP SWITCH

NOTE(S): EACH NAND GATE IS 1/4

OF A SN74LS00N

DIP SWITCH

SN74LS85N

SN74LS85N

SN74LS85N

HALL B

SN74LS85N

SN74LS85N

SN74LS85N

DIP SWITCH

5 KΩ

+5 V

0-11

ADDER

5 KΩ

NOTE(S): EACH NAND GATE IS 1/4

OF A SN74LS00N

Drawing 4

Drawing 5

DIP SWITCH

DIP SWITCH

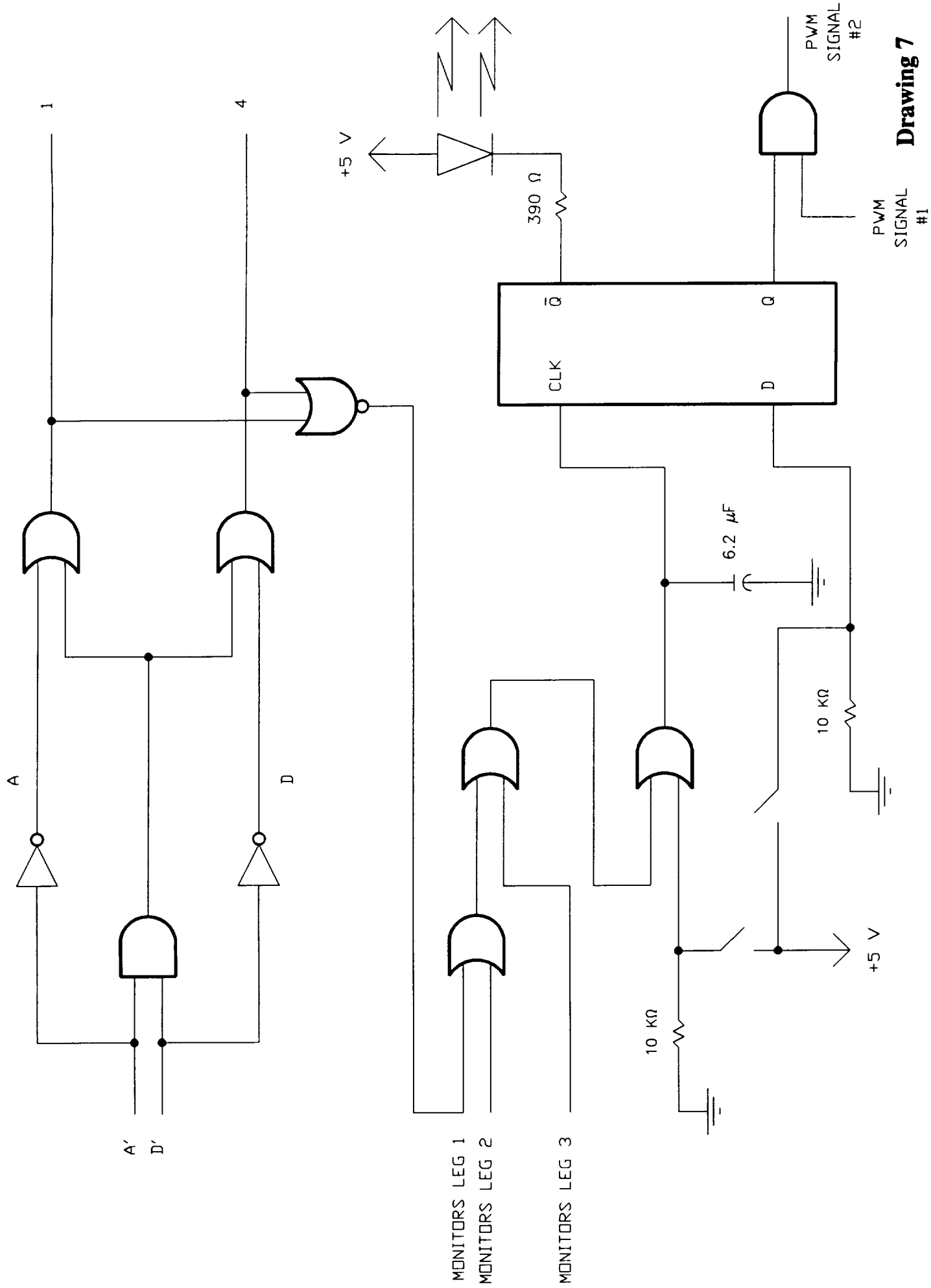SN74LS85N

HALL C

ADDER

0–11

+5 V

5 KΩ

5 KΩ
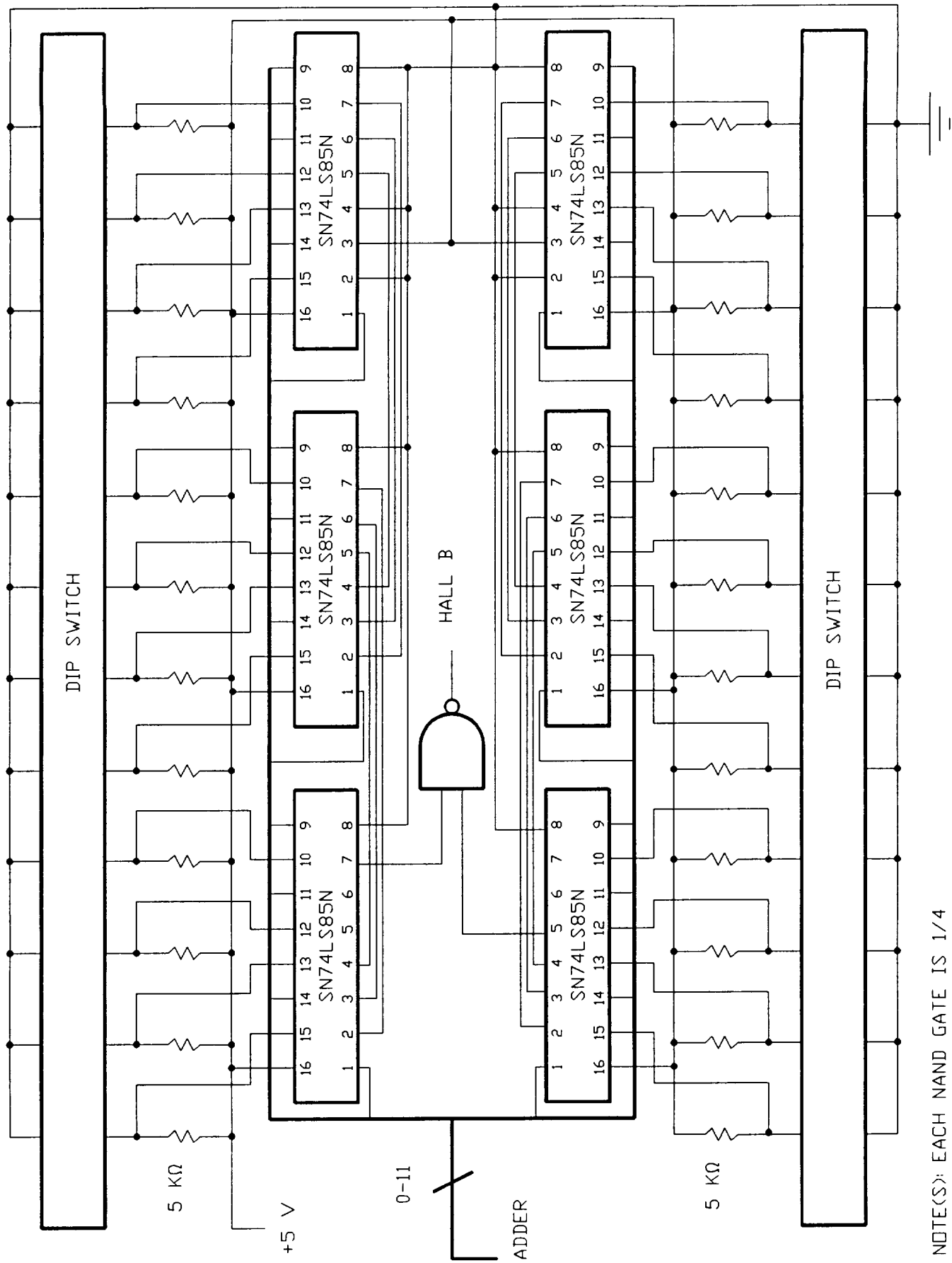
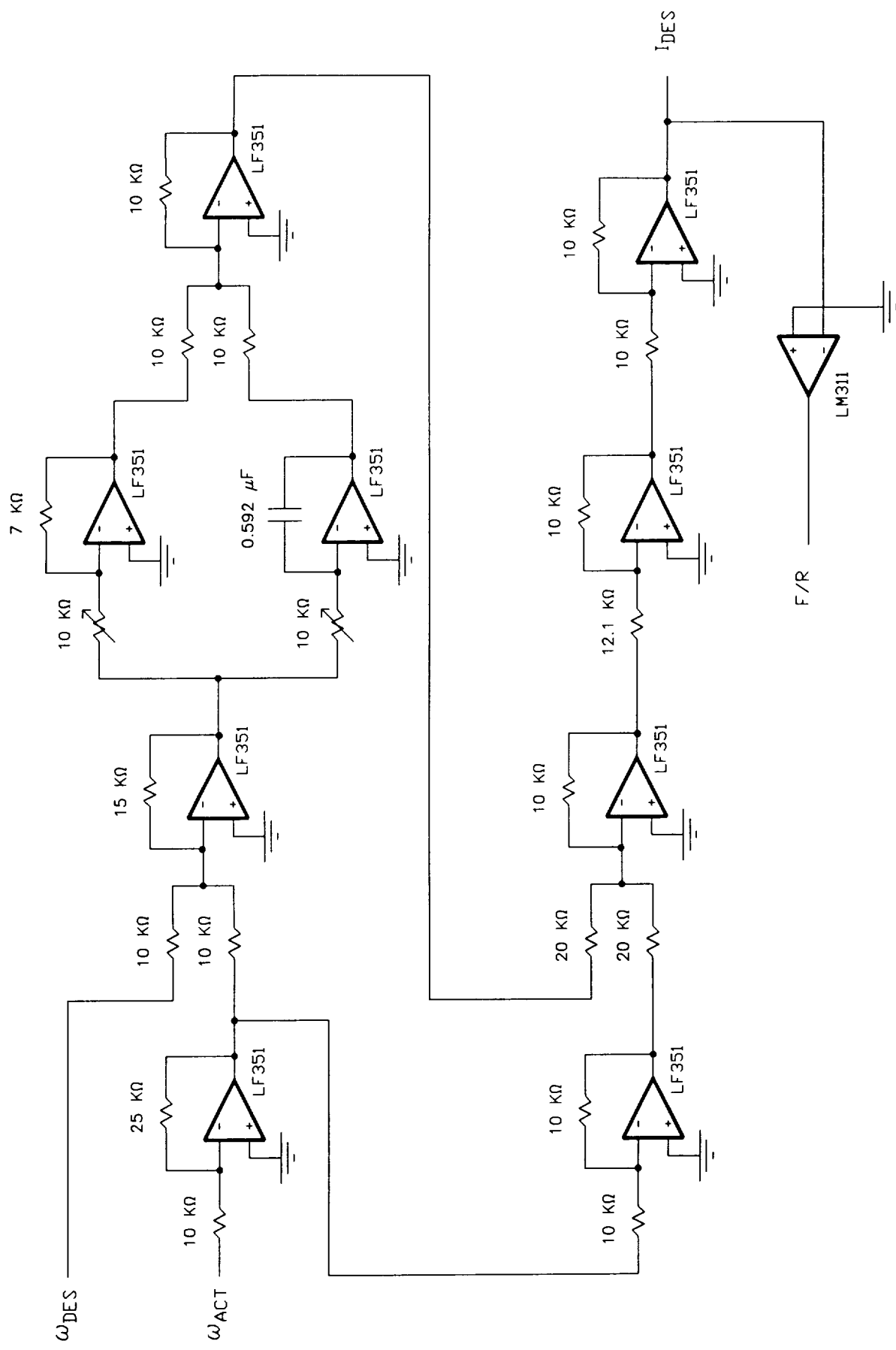NOTE(S): EACH NAND GATE IS 1/4

OF A SN74LS00N

Drawing 6

NOTE(S): (1) EACH NAND GATE IS 1/4 OF A SN74LS00N, (2) EACH OR GATE IS 1/4 OF A SN54LS32N, AND (3) EACH AND GATE IS 1/4 OF A SN54LS08N

Drawing 7

Drawing 8

Drawing 9